	WP6 CryoAC trade-off	**Doc. no. :** AHEAD-WP6-REP-004-2016 **Issue :** 1 **Date :** 03/10/2016 **Cat :** **Page :** 1 of 38

Title : **WP6: CryoAC trade-off**

Prepared by:	C. Macculi, F. Gatti, M. D'Andrea, M. Biasotti, D. Corsini, S. Lotti	Date:	28 September 2016
Inputs by:	L. Piro	Date:	21 September 2016
Checked by:	Jan-Willem den Herder	Date:	21 September 2016
PA agreed by:		Date:	
Authorised by:		Date:	

Distribution

AHEAD WP6 leaders
AHEAD management team

Document Change Record:

Issue	Date	Changed Section	Description of Change

Contents

Applicable Documents

[AD#]	Doc. Reference	Issue	Title
AD1	AHEAD consortium agreement	15-06-2015, final version	Integrated Activities for the High-Energy Astrophysics Domain, consortium Agreement

Reference Documents

RD#	Doc. Reference	Issue	title
RD1	SPIE SPIE Vol. 9905 99052F-1	2016	The Athena X-ray Integral Field Unit
RD2	SPIE Vol. 9905 99052K-1	2016	The Cryogenic AntiCoincidence Detector for ATHENA X-IFU: a program overview.
RD3	G.W Fraser, Cambridge Astrophysics Series		X-ray detectors in astronomy.
RD4	C.T. Chantler, et al.,NIST, Physical Measurement Laboratory		Detailed Tabulation of Atomic Form Factors, Photoelectric Absorption and Scattering Cross Section, and Mass Attenuation Coefficients for Z = 1-92 from E = 1-10 eV to E = 0.4-1.0 MeV.
RD5	arXiv: 1001.2110v2	2010	INTEGRAL hard X-ray spectra of the cosmic X-ray background and Galactic ridge emission.
RD6	Proc. SPIE 9905, DOI: 10.1117/12.2232381		Updates on the background estimates for the X-IFU instrument onboard of the ATHENA mission
RD7	arXiv: 0809.5018		5 years of survey on the Crab Nebula with SPI/INTEGRAL.
RD8	strawman_obsplan_athena_v2-7	2.7	Athena Mock Observation plan.
RD9	E. Cosulich et al.Nuclear Physics A 592 (1995) 59.	1995	The β decay of 187-Re studied with a cryogenic μ-calorimeter.
RD10			
RD11			
RD12			
RD13			

Abbreviations and acronyms

Item	Meaning
AHEAD	Integrated Activities for the High-Energy Astrophysics Domain
CSIC	

SRON	SRON Netherlands Institute for Space Research
TBC	To Be Confirmed
TBD	To Be Determined / Defined
VTT	
X-IFU	X-ray Integral Field Unit
INAF	Italian National Research for Astrophysics

1   Introduction

In this document we will report the feasibility study for the CryoAC detection capability in the hard X-ray energy bandwidth.

The main effort has been in understanding how the present "baseline" CryoAC detector can be improved or modified in order to enlarge scientific capability of the X-IFU instrument on energy bandwidth wider than the TES-array detector.

The solution here proposed are beyond the CryoAC baseline detector design, being this instrument not a spectroscopic one since it mainly works as anticoincidence particle detector.

This study starts with a brief overview of the CryoAC detector in order to know what is the baseline configuration which is the reference to start the feasibility study (Section 2).

Then, we will report a scientific assessment of the CryoAC starting with the evaluation of the minimum detectable flux followed by an evaluation of the scientific performance by simulations taking into account astronomical sources (Section 3).

The outcome of this scientific assessment will be the detector requirements enabling the CryoAC high energy scientific capability, whose parameters will be then probed in the related technological study (Section 4). The impact of the technological solution at the ATHENA X-IFU system level is reported in Section 5. Finally conclusions for the 2nd phase in the project are drawn.

In this report we present the trade-off analysis performed for the cryogenic Anti-Coincidence detector (CryoAC). Whereas the detailed optimization of the detector is done as part of the X-IFU instrument design, within the context of AHEAD two major improvements are under study:

- increase of the solid angle sensed by the CryoAC
- improvement of the high energy response of the CryoAC to provide additional science return for high-energy photons (> 12 keV)

As the second item may directly influence the physical properties of the cryoAC the current trade-off has been focussed on this part to be able to consider changes needed for the high energy response in the further work in this work package.

The work here presented reshuffle a bit the workflow with respect to the AHEAD proposal by giving now a more reasonable and robust path toward the same goal.

For reference we give in the introduction the WP description from the AHEAD consortium proposal (AD1: Call H2020-INFRAIA-2014-2015, proposal SEP-210187231). The AHEAD proposal lists under WP 6.4 the following for the cryogenic Anti-coincidence detector:

WP 6.4: **Anti-coincidence detectors (AC):**
UniGenoa, INAF/IAPS-RM and SRON

Rejection of the in-orbit particle background by a factor of 100 or more is required to carry out measurements of faint or diffuse X-ray sources. This reduction can be achieved with an anticoincidence

detector (AC) that needs to be close to the microcalorimeter, and therefore operated at similar low temperatures. The baseline AC detector is based on a Si absorber read-out by a distributed set TES sensors and its performance has been demonstrated (ref. 3). This concept has several advantages: a low energy threshold, the possibility to disentangle the thermal from a-thermal signal components, the same operating temperature and the SQUID readout similar to the main detector. This work package includes three relevant sub-workpackages:

a) *optimization of size of the anti-co detector*
b) *application of additional anti-co detectors to cover the lateral sizes of the sensor*
c) *feasibility study of detection capability in the hard X-ray band*

In the current design the size of the anti-co is 1 mm larger than the sensor (18 mm compared to 17 mm). Together with a typical distance of 1 mm this implies that on the outer pixels particles with an incident angles greater than 63° may be missed by the anti-co detector (depending on the direction of the particle). Clearly a larger anti-co will improve this and an increase of the anti-co size by 3 mm already improves this by a factor 2. As the first task we expect to demonstrate the feasibility of such devices. A further improvement can be obtained by adding a number of pixels covering the lateral edges of the detector. This requires optimized pixels for this purpose as well as a proper design of the focal plane assembly.

Another improvement of the anti-coincidence detector is its use as a hard X-ray detector (E>20 keV). This enables, in combination with the top-layer microcalorimeter array, the simultaneous measurement of X-ray spectral features over a broad energy range. There are numerous science goals that will benefit (e.g. the simultaneous study of the iron line and hard X-ray reprocessing component produced by an accretion disk around a black hole). In the first phase we will study the science requirements, in particular the energy band. This could require a detector design for achieving the selected stopping power. After a preliminary design phase, one or two geometries and materials could be investigated and tested at 50 mK prior to the fabrication and the test of a demonstrator. This study will give all the science and detector parameters for a design and fabrication of such detector in view of an application to space based observations. Based on these results a decision will be taken on the feasibility to include this additional feature in the X-IFU on Athena.

This work has a strong link to WP 9 which will provide detailed estimates of the different background components (cosmic rays, particles with a solar origin, etc.). The devices will be produced in available production facilities at the University of Genova and tested at INAF/IAPS-Roma. The EU funding will allow us to demonstrate the improved performance.

The relevant deliverable addressed in this report is given below [AD1]:

Number	Name	Short name	Type	Dissemi-nation level	Delivery date
6.3	Design trade off report: cryoAC	INAF/IAPS	R	CO	12

2   Functional description of the cryogenic Anti-Coincidence detector

The ATHENA observatory is the second large-class ESA mission, in the context of the Cosmic Vision 2015 - 2025, scheduled to be launched on 2028 at L2 orbit. One of the two on-board instruments is the X-IFU (X-ray Integral Field Unit): it is a TES-based kilo-pixels order array able to perform simultaneous high-grade energy spectroscopy (2.5 eV at 6 keV) and imaging over the 5 arcmin FoV. The X-IFU sensitivity is degraded by the particles background which is induced by primary protons of both solar and Cosmic Rays origin, and secondary electrons. The studies performed by Geant4 simulations depict a scenario where it is mandatory the use of reduction techniques that combine an active anticoincidence detector and a passive electron shielding to reduce the background expected in L2 orbit down to the goal level of 0.005 cts/cm^2/s/keV, so enabling the characterization of faint or diffuse sources (e.g. WHIM or Galaxy cluster outskirts).

From the detector point of view this is possible by adopting a Cryogenic AntiCoincidence (CryoAC) placed within a proper optimized environment surrounding the X-IFU TES array.

The detector is divided into 4 independent trapezoidal pixels (see Fig. 1), each one having an area of 1.15 cm^2, connected to a silicon rim by 3 bridges per pixel in order to realize the thermal conductance to the thermal bath. The baseline design is based on absorbers made of a thin single Silicon crystal (500 μm thick), where the energy deposited by particles is sensed by Iridium TES detectors. The CryoAC is placed below the TES-arrays, at a distance < 1 mm. The active part covers a full area of 4.6 cm^2, larger than the arrays (2.6 cm^2). See [RD1, RD2] and Refs. therein for a more detailed scenario.
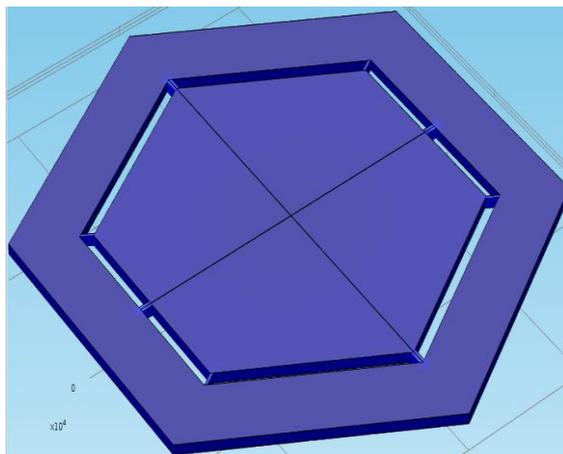
Fig. 1 - The CryoAC detector schematic: 4 trapezoidal silicon pixels connected to a silicon rim by 3 bridges per pixel. On each absorber will be deposited a network of about 100 TES (here not shown).

This represents the starting point of the feasibility study.

3 Determination of the main parameters to address the CryoAC towards a hard X-ray detector

The aim of this section is to provide the detector requirements that will be the base of the technological feasibility study.

It starts with the evaluation of the minimum detectable flux by considering the baseline CryoAC design (500 μm of Silicon absorber), followed by scientific simulations of astronomical observations whose results are based on variation of detector parameters (i.e., energy resolution).The section will be concluded by the assessment of the requirements to move the present baseline detector to a "design" for having detection capability in the hard X-ray energy bandwidth.

3.1 *Scientific Assessment of the CryoAC: the minimum detectable flux.*

In general, in order to properly design a detector in the X-ray band, one of the necessary parameter to evaluate is its "minimum detectable flux". This parameter characterizes the detector performances in terms of signal to noise ratio, determining the instrument sensitivity and then the suitable astronomical targets.

The minimum detectable flux F_{MIN} within an observing time t and a ΔE energy band can be expressed as RD3:

$$F_{MIN} = \frac{n_\sigma}{Q \cdot A_{eff}} \sqrt{\frac{B_P \cdot A_D + Q \cdot j_d \cdot \Omega \cdot A_{eff}}{t \cdot \Delta E}} \quad \frac{[cts]}{[cm^2 \cdot s \cdot keV]} \tag{1}$$

where n_σ is the desired confidence level (i.e. $n_\sigma = 3$ corresponds to 99.8% confidence), Q is the detector response function ([counts/photons]), A_{eff} and A_D are respectively the detector effective and geometric areas ([cm^2]), Ω is the angular size of the observed source in [sr] (i.e. for point sources the instrument angular resolution), B_P is the internal particle background level ([cts]/[cm^2 s keV]) and j_d the flux of the diffuse component of the background ([ph]/[cm^2 s keV sr]).

In the next sub-section we will evaluate all the parameters above reported, considering the baseline CryoAC design.

3.1.1 *CryoAC response function*

The CryoAC response function has been estimated by means of a Monte Carlo simulation, using the Geant4 toolkit. The simulation included a simplified model of the X-IFU FPA, taking into account the photons absorption due to the thermal filters (0.21 μm of Aluminium and 0.28 μm of Polymide) and the TES array (1 μm of Gold and 4 μm of Bismuth); and the photoelectric absorption efficiency in the CryoAC Silicon absorber (thickness: 500 μm). The result is shown in Fig. 2.
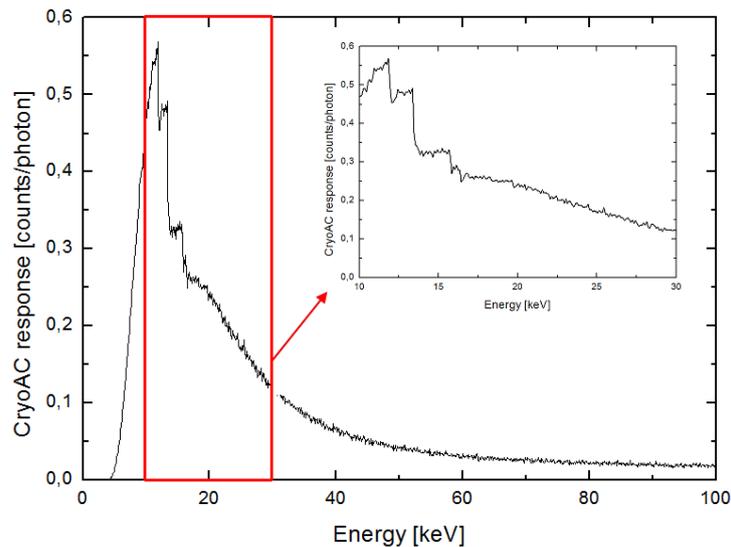
Fig. 2- CryoAC response function estimated by means a Geant4 simulation. The red box highlights the 10 - 30 keV energy band (encapsulated plot).

The response function rapidly grows at low energy, it shows a maximum around 12 keV (Q_{MAX} = 0.57) and decreases at higher energies, dropping below the 0.10 level above 30 keV.

To understand the contribution of the different elements in the FPA to the CryoAC response, in Fig. 3 are reported the transmission curves of the respective materials estimated using the X-ray attenuation coefficients tabulated by NIST RD4. In the same plot is also shown the absorption curve of the CryoAC Silicon absorber.
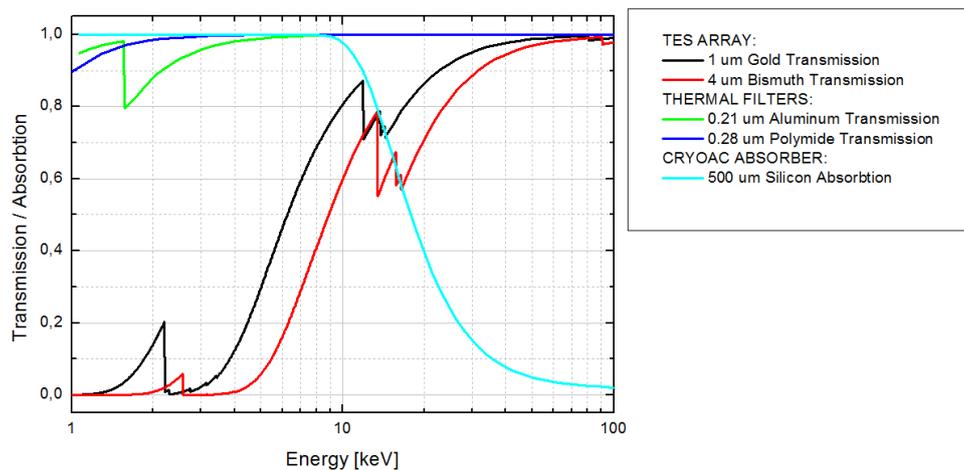
Fig. 3 - Different contributions to the CryoAC response function estimated using the attenuation coefficients from the "NIST X-ray Form Factor, Attenuation, and Scattering Tables" [Ref.].

Fig. 3 - Different contributions to the CryoAC response function estimated using the attenuation coefficients from the "NIST X-ray Form Factor, Attenuation, and Scattering Tables" [Ref.].

It is clear that below 10 keV the behavior of the response function is dominated by the photon absorption in the TES array, whereas above 30 keV the dominant contribution is the quantum efficiency of the CryoAC absorber. In the intermediate energy range the two contributions are roughly equivalent.

3.1.2   ATHENA effective area

Prof. R. Willingale (ESA ATHENA Telescope Working group) has provided us the on-axis effective area of the ATHENA telescope in the range 10-30 keV (Fig. 4). The data refers to mirrors with nominal Iridium coating density and a surface roughness of 5 Å.
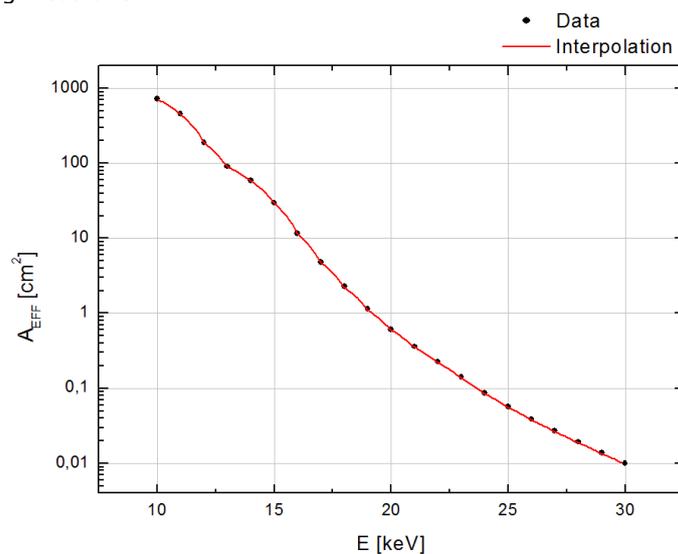
Fig. 4- On-axis effective area of the ATHENA telescope for nominal Iridium coating density and a surface roughness 5 Å rms. The red line is an interpolation of the data provided by the ESA ATHENA Telescope Working group (black points).

As shown in Fig. 4, in this energy range the effective area rapidly drops and hits the value of ~ 1 cm^2 around an energy of 18 keV.

Based upon this data, we can conclude that within the ATHENA context the target hard X-ray band is limited in the range $10 \div \sim 20$ keV. As shown in the previous section (Fig. 3), the current CryoAC design ensure a good quantum efficiency at these energies ($Q_{500\mu m\ Si,\ 20keV} \sim 40\%$), and so we do not consider useful to put effort into an upgrade of the absorber characteristics (i.e. the thickness or the material) at this stage.

3.1.3   Photon and particle background

In this subsection we will present the estimates of the background sensed by the CryoAC in the X-IFU FPA.

3.1.3.1 Diffuse X-ray background

The diffuse component of the background has been estimated starting from the hard X-ray spectrum of the Cosmic X-ray Background (CXB) measured by IBIS/INTEGRAL. To modelling this spectrum we used its analytical description proposed by M. Turler et al. [RD5]:

$$E^2 j_d(E) = E^2 \frac{dN_\gamma}{dE} = E^2 \frac{0.109 \; ph \; cm^{-2} s^{-1} keV^{-1} sr^{-1}}{(E/28 \; keV)^{1.40} + (E/28 \; keV)^{2.88}} \tag{2}$$

A plot of the model is shown in Fig. 5.
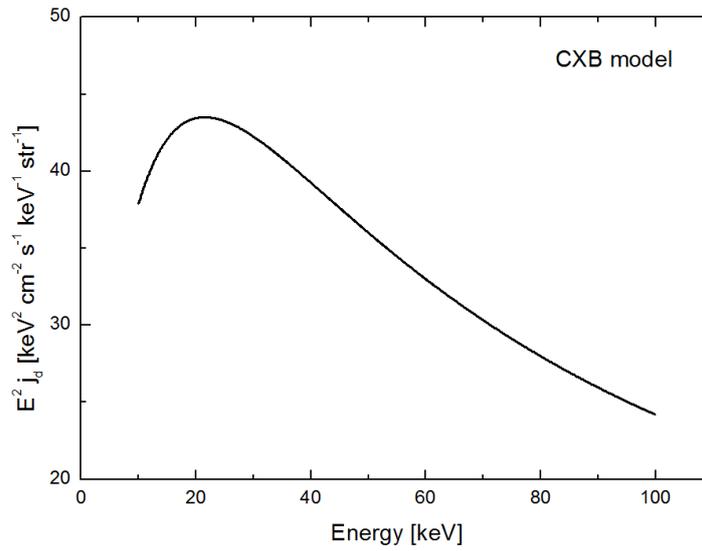
Fig. 5- Model of the CXB hard X-ray spectrum [RD5].

To obtain the diffuse X-ray background level this flux must be multiplied by the detector aperture Ω and folded with the detector response function Q(E) [RD3]:

$$B_x(E) = Q(E) \cdot j_D(E) \cdot \Omega \; \; [cts]/[cm^2 \; s \; keV] \tag{3}$$

Considering a single CryoAC pixel the aperture is given by:

$$\Omega = \frac{A_D}{f_L^2} = 0.80 \cdot 10^{-6} \; sr \tag{4}$$

where $A_D = 1.15 \; cm^2$ is the geometric area the pixel, and $f_L = 12 \; m$ is the focal length of the ATHENA telescope. Note that this aperture corresponds to a FOV of $9.4 \; arcmin^2$ for a single CryoAC pixel.

3.1.3.2 *Internal particle background*

The internal particle background has been estimated by means of a Monte Carlo simulation, using the Geant4 toolkit. The simulation reproduces the L2 environment and the ATHENA mass model (see [RD6] for details), and it takes into account the use of the X-IFU TES array as "reverse" anticoincidence device. This is the opposite of what happens in observations with the X-IFU, where it is the CryoAC that discriminates main detector events that happen in both detectors. In this context is the main detector that can act as an anticoincidence device for the CryoAC, reducing the particle background to some extent despite not being designed/optimized for the scope.

The estimated residual background spectrum is shown in Fig. 6.
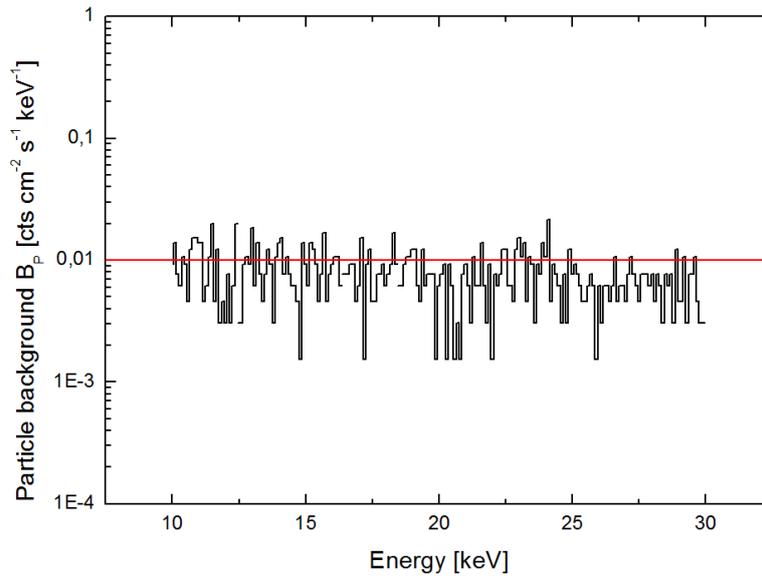
Fig. 6- Spectrum of the residual particle background expected on the CryoAC.

The particle background level is roughly constant in the 10-30 keV energy band, and so we can consider:

$$B_P(E) = B_P \sim 0.010 \ [cts]/[cm^2 \ s \ keV] \tag{5}$$

3.1.3.3 *Total background*

The resulting total background level is given by [RD3]:

$$B_{TOT}(E) = B_P(E) \cdot A_D + B_x(E) \cdot A_{eff}(E) \quad [cts]/[s \ keV] \tag{6}$$

The relative spectrum in the band 10-30 keV is shown in Fig. 7.
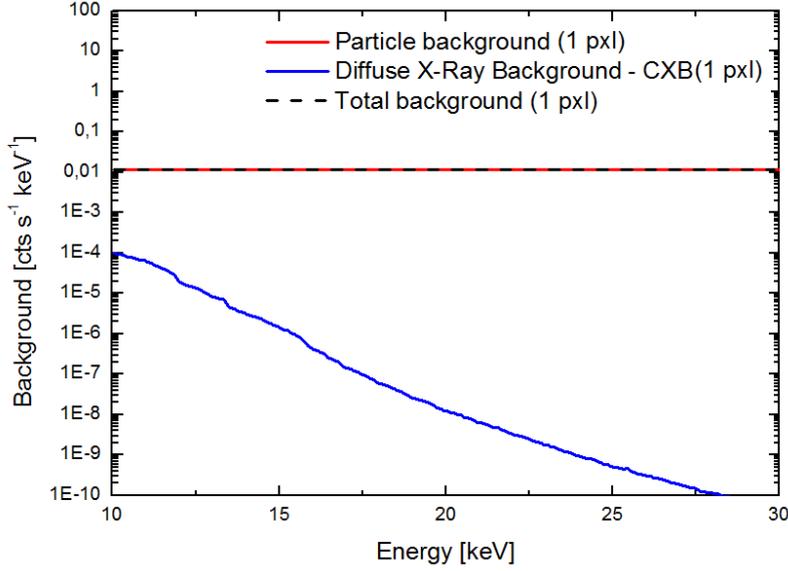
Fig. 7- Spectra of the particle, diffuse and total background expected on a CryoAC pixel.

Note that at these energies the diffuse X-Ray component of the background is always negligible with respect to the internal one, and so it can be neglected in this study.

3.1.4 Minimum detectable flux

Including in eq. (1) the energy-dependence of Q and A_{eff}, and neglecting the diffuse X-ray background contribution, the minimum detectable flux can be expressed as:

$$F_{MIN} = \frac{n_\sigma}{\int_{Emin}^{Emax} Q(E) \cdot A_{eff}(E)\, dE} \sqrt{\frac{\int_{Emin}^{Emax}(B_P(E) \cdot A_D)\, dE}{t}} \quad \frac{[cts]}{[cm^2 \cdot s \cdot keV]} \qquad (7)$$

Using the parameters evaluated in the previous sections, we have estimated F_{MIN} for a CryoAC pixel, assuming a desired 5σ confidence level.

In Fig. 8 the limit flux is reported as a function of the observation time in different energy ranges, whereas in Fig. 9 is shown as a function of energy, assuming a 100 ks exposure and a bandwidth ΔE=E.
These two plots characterize the sensitivity of the CryoAC pixels to a continuum emission, showing that the limiting fluxes with the baseline detector design are fractions of mCrab in the band 10 ÷ ~20 keV. We point out that this energy range is not limited by the detector efficiency, but it is due to the sharp drop of the ATHENA effective area at high energies.
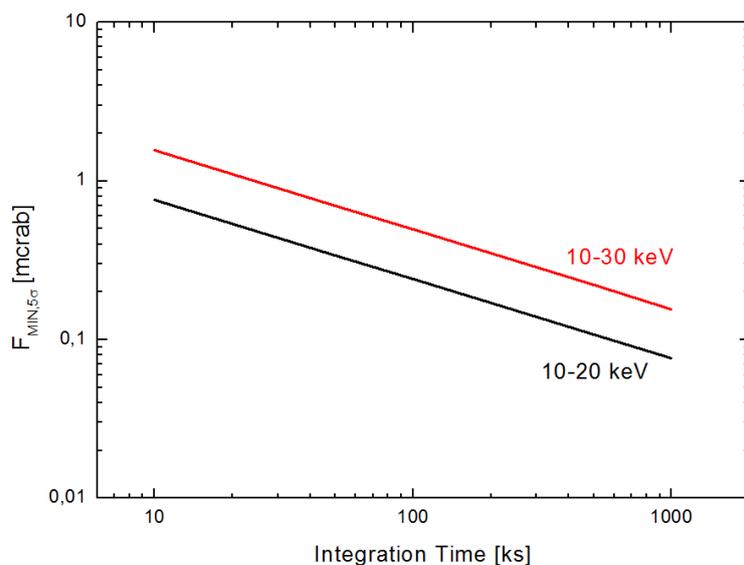
Fig. 8- CryoAC minimum detectable flux as function of the observation time.
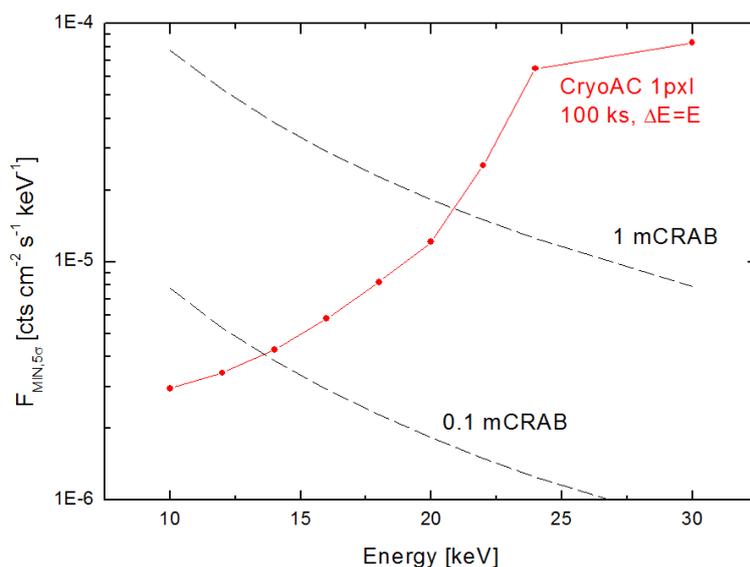
Fig. 9- CryoAC continuum sensitivity for 100 ks of exposure time and an energy bandwidth ΔE=E. Crab fluxes are overplotted as reference.

3.2 Scientific Simulations

In this section we will present some scientific simulations of astronomical targets that we have performed with the XSPEC software in order to understand the CryoAC spectroscopic capabilities.

3.2.1   Crab observation

First, we have simulated a 100 ks observation of the Crab Nebula.
To model the Crab spectrum we have used a power law with photon index *α = 2.08* and normalization *K = 9.3 [ph]/[cm² s] at 1 keV* [RD7].

The ATHENA effective area, the background spectrum and the detector response function estimated in the previous section have been converted into the XSPEC format. We have generated several response matrices, varying the ΔE in the range 2 ÷ 20 keV (FWHM). The spectra of the Crab simulated accounting for the different energies resolutions are shown in Fig. 10.

We fitted the simulated dataset in order to assess the accuracy by which the source parameter could be recovered. To fit the spectra we have used the *grppha* routine to rebin the data until each bin has a minimum of 30 counts. The results of the fit are shown in Table 1, where we have reported the 90% confidence range of the spectral parameter obtained with the different energy resolutions.
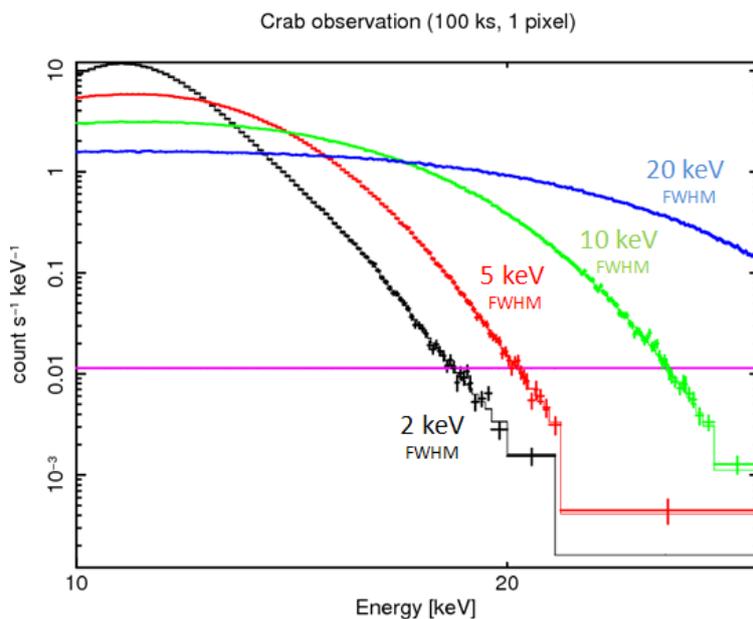
Fig. 10- Crab spectra for a 100ks observation with a CryoAC pixel and different values of the energy resolution. The violet line represents the background level.

Energy resolution (FWHM)	α 90% confidence range	$\frac{\Delta\alpha}{\alpha}$	K ([ph]/[cm² s]) 90% confidence range	$\frac{\Delta K}{K}$
2 keV	2.07 ÷ 2.10	1.4%	9.1 ÷ 9.8	7.2%
5 keV	2.06 ÷ 2.12	2.8%	8.8 ÷ 10.2	15%
10 keV	2.05 ÷ 2.18	6.8%	8.6 ÷ 12.0	36%
20 keV	2.10 ÷ 2.51	20%	9.8 ÷ 26	174%

Table 1- Spectral parameter of the Crab Nebula obtained simulating a 100 ks observation with the CryoAC for different values of the energy resolution.

It is important to note that the spectral resolution deeply influences the performances of the CryoAC, significantly conditioning the errors on the parameters determination. Based upon these results, we can conclude that an energy resolution of few keV (FWHM) is necessary to address the CryoAC toward an Hard X-ray detector.

3.2.2   HXRBs observation

To evaluate the CryoAC scientific capabilities and the role of its energy resolution also in combination with the TES array, we have simulated the observation of High-mass X-ray binary (HMXB) spectra with both the instruments. These sources can present a high energy cut-off in the CryoAC energy bandwidth (10 ÷ 20 keV), and so they represent an interesting target in the context of this trade-off study.

For the HMXB spectra we have used a simplified model with an absorbed power law spectrum and a high energy cut-off (wabs*highecut*powerlaw in XSPEC), generating several models with different cutoff energies in the range 8-16 keV. The parameters are given in Table 2, and the models are shown in Fig. 11.

Component	Parameter	Value
wabs	N_H	2·10²² cm²
highecut	E_C	8, 10, 12, 14, 16 keV
highecut	E_F	10 keV
powerlaw	Γ	1.5
	Flux 0.2 - 20 keV	100 mCrab

Table 2- HMXB models parameters.

Models wabs*highecut*pow
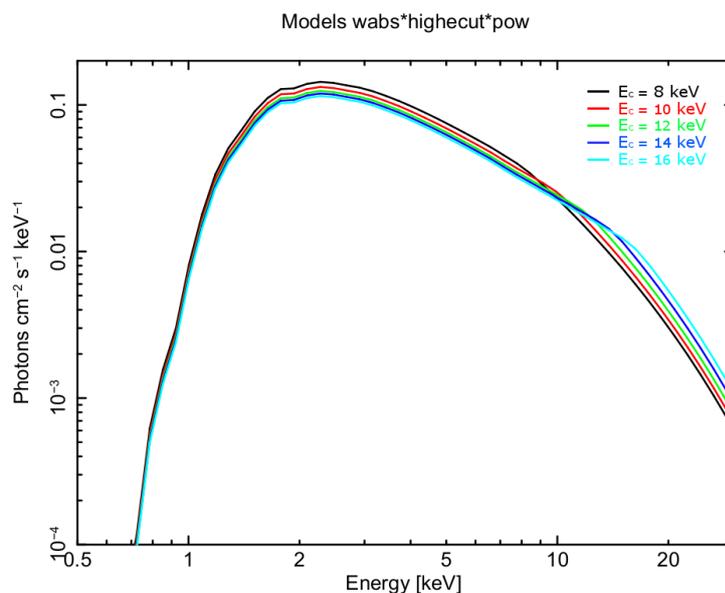
Fig. 11- HMXB spectral models.

For each model, we have simulated three different observations:

- 50 ks exposure with the X-IFU TES Array
- 50 ks exposure with both the X-IFU TES Array and the CryoAC (energy resolution ΔE=2keV FWHM)
- 50 ks exposure with both the X-IFU TES Array and the CryoAC (energy resolution ΔE=5keV FWHM)

An example of simulated spectrum is shown in Fig. 12.

In Tab. 3 are reported the high energy cut-off parameters obtained fitting the simulated spectra. The use of the CryoAC as hard X-ray detector allows to improve the characterization of the cut-off and the folding energies of the sources for E_C>10 keV, whereas the TES array is unable to properly constrain them. Furthermore, note that also in this case the energy resolution of the CryoAC plays a fundamental role in the parameter characterization, significantly influencing the instrument performances.

HMXB observation (50 ks, Flux 0.2−20 keV = 100 mCrab)
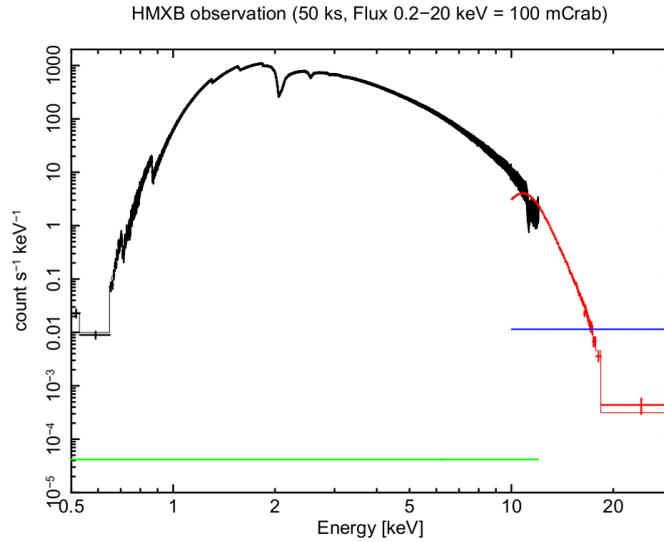
Fig. 12- HMXB spectrum with a cut-off at EC=12keV observed with both the X-IFU TES array (black data) and the CryoAC (red data). The green and the blue lines represent respectively the TES array and the CryoAC background levels.

MODEL	TES ARRAY	TES ARRAY + CRYOAC (ΔE = 2 keV FWHM)	TES ARRAY + CRYOAC (ΔE = 5 keV FWHM)
$E_C=8$ keV	$E_C = 8.01^{+0.02}_{-0.02}$ keV $E_F = 9.60^{+0.11}_{-0.11}$ keV	$E_C = 8.00^{+0.02}_{-0.01}$ keV $E_F = 9.63^{+0.11}_{-0.11}$ keV	$E_C = 8.00^{+0.02}_{-0.01}$ keV $E_F = 9.61^{+0.11}_{-0.11}$ keV
$E_C=10$ keV	$E_C = 9.97^{+0.04}_{-0.03}$ keV $E_F = 8.88^{+0.17}_{-0.43}$ keV	$E_C = 9.93^{+0.03}_{-0.03}$ keV $E_F = 9.47^{+0.25}_{-0.24}$ keV	$E_C = 9.94^{+0.03}_{-0.03}$ keV $E_F = 9.31^{+0.35}_{-0.35}$ keV
$E_C=12$ keV	$E_C = 9.2^{+0.3}_{-0.5}$ keV $E_F = 113^{+54}_{-30}$ keV	$E_C = 11.6^{+0.2}_{-0.2}$ keV $E_F = 12.0^{+1.5}_{-1.5}$ keV	$E_C = 11.0^{+0.2}_{-0.2}$ keV $E_F = 19.1^{+4.0}_{-3.0}$ keV
$E_C=14$ keV	$E_C = 9.3^{+0.4}_{-0.5}$ keV $E_F = 155^{+80}_{-39}$ keV	$E_C = 13.4^{+0.5}_{-0.5}$ keV $E_F = 15.3^{+7.1}_{-4.7}$ keV	$E_C = 14.7^{+2.0}_{-1.5}$ keV $E_F = 4.3^{+11.2}_{-4.3}$ keV
$E_C=16$ keV	$E_C = 8.1^{+0.8}_{-1.0}$ keV $E_F = 248^{+170}_{-93}$ keV	$E_C = 14.3^{+0.9}_{-1.2}$ keV $E_F = 23^{+39}_{-12}$ keV	$E_C = 8.0^{+0.6}_{-1.0}$ keV $E_F = 261^{+190}_{-79}$ keV

Table 3- High energy cut-off parameters obtained fitting the simulated spectra in the different configurations. The errors refer to the 90% confidence level.

To evaluate the relevance of this study case in the context of ATHENA, we have analyzed the last Mock Observing Plan [RD8] searching for sources with characteristics similar to the ones we have simulated. Within the X-IFU observations, we have found:

- 25 X-Ray Binaries with average source intensity $F_{AVG} \geq 100$ mCrab and planned exposure time t = 20 ks
- 10 X-Ray Binaries with 10 mCrab $\leq F_{AVG} < 100$ mCrab and planned exposure time in the range t = 20 ÷ 200 ks

As we have seen the use of the CryoAC as "spectroscopic" X-ray detector could bring to an extension of the X-IFU energy range until ~20keV, and an optimization of the instrument energy resolution around ΔE ~ 2keV could allow to characterize these sources in this enlarged band. Thus it is interesting to probe this "spectroscopic" function of the CryoAC by a technological study.

3.3 Requirements

The results from the previous section indicate that the CryoAC can operate as hard X-ray detector only in a narrow energy band (10 ÷ ~20 keV), limited by the effective area of the ATHENA telescope.
We have presented a study case regarding the observation with both the X-IFU TES array and the CryoAC of X-ray Binary systems. In the ATHENA Mock Observing Plan there are about 35 sources with characteristics similar to the ones we have simulated. This means that we could have an interest from the scientific point of view in trying to optimize the CryoAC energy resolution. The required value that we have identified is 2 keV (FWHM).

In the next section we will address how it is possible to satisfy this requirement from the technological point of view, by taking into account that the CryoAC for ATHENA X-IFU is designed as not spectroscopic detector being this feature not required in the baseline design.

4   Technological Study of the detector

We are here considering an improvement of the baseline, non-imaging detector having an active area of several square centimetres operating at about 50-70 mK and located beneath the soft-Xray microcalorimeter array on the focal plane of the X-ray optics. This is the configurations of the proposed X-IFU instrument, in which a large area detector for GeV charged particle of the cosmic rays is designed for only anticoincidence purpose.

We are proposing to investigate 3 new lines of investigation for extending its operation to hard X-ray. This could be followed by an experimental assessment of the selected number of new detector configurations. We will revisit the present configuration of anticoincidence detector in order to include "ad hoc" modification to realize the wanted sensitivity to the hard X-ray with a reasonable good spectral performance together with high counting capability. The design must be compatible with the anticoincidence performance previously settled by the mission. This means that the detection of Hard X-ray wouldn't affect the anticoincidence operation and efficiency and, if possible, it can provide a good "per se" discrimination among the two types of events: charged particles from Hard X-rays event.

Here we present the preliminary phase of the study of a such new multipurpose detector. The investigation moves on 2 design concepts that will be described in the following section.

In particular, we propose 2 main lines of development that we call Concept Design #1 (CD#1) and Concept Design #2 (CD#2). The CD#1 is based on a re-assessment approach of the present non spectroscopic design with consequent small number of modifications and maximal readiness level, while the CD#2 will be based on a maximal goals accomplishment level approach with consequent large modifications and, consequently, possible lower readiness level. Both concept designs have to meet the requirements:

- X-ray energy band: 10-20 keV
- X-ray absorption efficiency: $\geq 40\%$
- energy resolution: better than 2keV FWHM

4.1   Concept design #1

The first proposal of the concept for Hard-Xray detection of the anticoincidence for the XIFU instrument for the ATHENA mission is based on minimal re-assessment of the present design.
The detector structure is based on silicon chip that acts as substrate and as absorber at same time. Energetic charged particles passing through the silicon substrate leave energy in form of electron-holes pairs and phonons. Part of the primary energy, about 3% to 5%, goes on high energy phonons that travels in quasi-ballistic way. This first phonon burst produced by the interaction with a charged particle is promptly detected by TESs that are grown on one surface. The energetic phonons that hit the TES's electron gas gives rise to a signal. In order to maximize the detection efficiency of the quasi-diffusive phonon burst emerging from the hot spot, we have uniformly distributed the TES on one silicon face. The whole sensing structure is composed by 65 TESs, each with 100×100 μm^2 area and 200-nm-thick Ir film. These are parallel connected and read as a single TES. The TESs readout connection is made by niobium wires. The thermal conductance is controlled by sizing 4 legs that are micro-machined in the silicon chip (Fig.13).
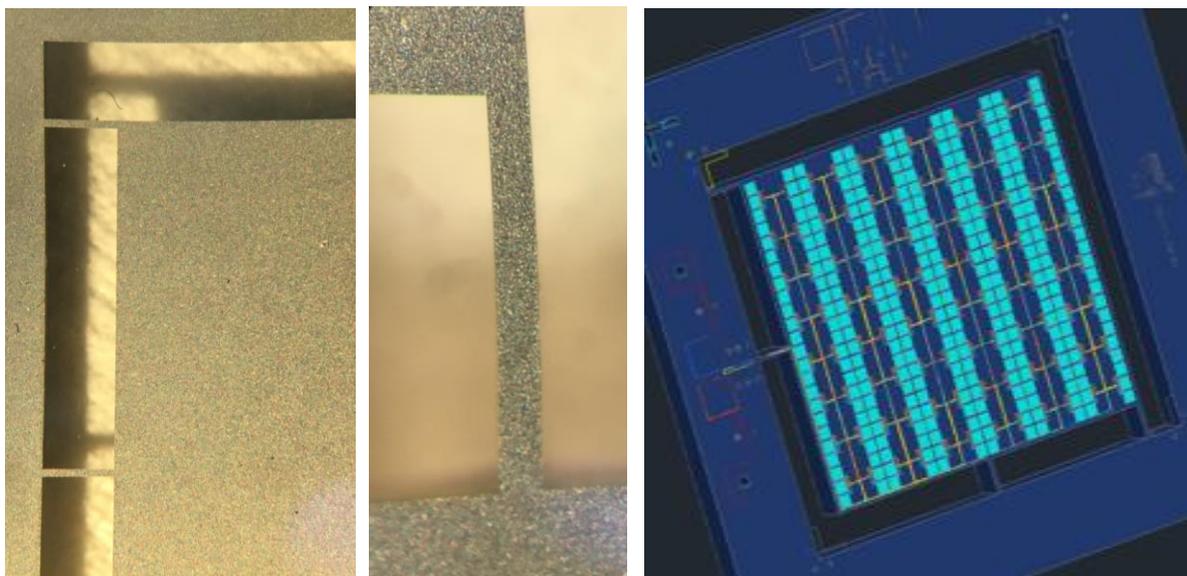
Fig. 13 - Two views of the anticoincidence chip for XIFU/ATHENA. Left: the upper left corner with the external rim, the 2 (100 um x 1 mm) bridges, the central active area. Centre: one bridge magnified with microscope (the apparent bending of the structure are caused by microscope-camera optics). Right: CAD drawing.

Preliminary prototypes have been built with provisional thermal conductance made of 4 SU-8 hollow towers filled with epoxy glue on top of a base silicon chip that works as "support". Those towers connect the backside of active chip to a "supporting" silicon chip that is mounted in strong thermal contact to the cryostat thermal bath. The shape of towers allows us to control the thermal conductance, which was expected to be 10^{-8} W/K. Measurements of prototypes down to 100 mK have confirmed these values as shown in Fig. 15. The anticoincidence detectors prototype has been produced at the Genova University (Phys. Dept.). The "active" part of the detector was fabricated in three steps. First, we have grown an iridium film on a commercial available silicon wafer, quality "electronic grade". The growth is performed by pulsed laser deposition (PLD) and the thickness obtained is typically 200 nm. Second, we have used positive photolithography and dry etching to pattern iridium film and to obtain 65 identical TESs on the silicon substrate. Dry etch is performed by ion milling using argon ion gun. In the last step, the Nb wiring: negative photolithography, niobium deposition by RF-sputtering and lift-off process have been used to grow niobium strips to connect all TESs. The fabrication parameters are summarized in table below:

Parameter	*Value*
Silicon Active Area	10x10 mm^2
Silicon Thickness	380 um
TES Area (x65) of Ir	100x100 um^2 (x 65)
TES Ir thickness	200 nm

Table 4– Fabrication parameters of preliminary prototype

A typical prototype device shows a critical temperature of 124 mK with a transition width of about 2 mK and a normal resistance of 2 mΩ. In Fig. 14 are reported some I-V curves at different temperatures across the

transition: the black line shows the curve at 124.25 mK corresponding ¾ of the full transition, where at large voltage bias a completely normal state is observed, whereas the green line is the measurement performed at 120.34 mK and corresponds to a full superconductive behaviour. The measurement presented with orange dotted line (123.79 mK) is characterized by instability (dotted region) probably due to a too high electro-thermal feedback. The resistance vs. temperature plot is obtained point by point fitting the linear low bias power region of the I-V curves at each base temperature. In the same plot is reported also the thermometric sensitivity Alpha , $\alpha=(T/R)(dR/dT)$, as function of temperature. Its maximum value is about 240. The uncertainty on the temperature measurements is 0.03 mK.
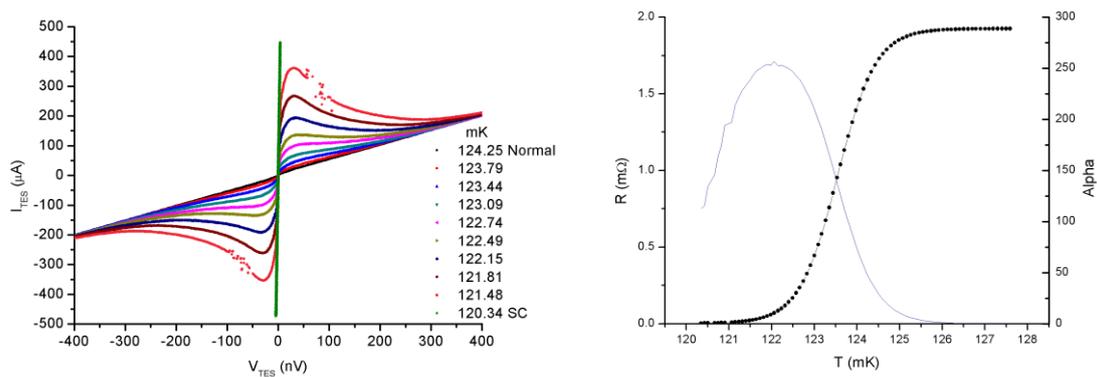
Fig. 14 - I-V Plot of the prototype device of the Anticoincidence having thermal conductance provided by 4 SU-8 epoxy towers.
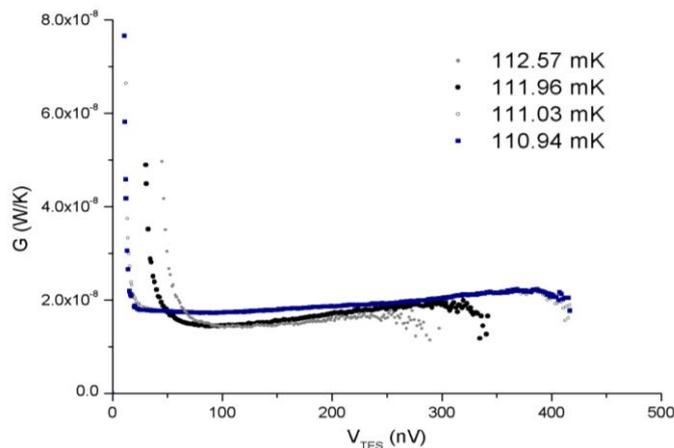
Fig. 15 - The thermal Conductance measurements at several base temperatures and at different voltage bias points. The average values, after cutting out the lowest and the highest bias points, stay from 1.8 and 1.9x10^{-8} W/K, less than a factor two from the expected one.

The energy resolution was tested with 60 keV gamma line from a [241]Am gamma source. Gamma rays emitted by americium are absorbed inside the silicon by photoelectron absorption. The 60 KeV photoelectrons have a range

of about 35 um in silicon and in this case simulate the loss of energy of GeV protons in silicon 380 um thick that is about 130 KeV (3.5 MeV/cm). The detected pulses can be fitted with two components: a faster one "a-thermal", due to quasi-ballistic phonons, and a slower one thermal. In Fig. 16 is shown a typical pulse with the two components fitted with exponential decay functions. The a-thermal component rise time is 24 µs whereas the thermal signal has a rise time of 190 µs. The decay time are 0.34 ms and about 12 ms respectively. The measured energy resolution at the Americium-241 60 KeV line is 11.3 KeV FWHM and 7.9 FWHM at 11 KeV.
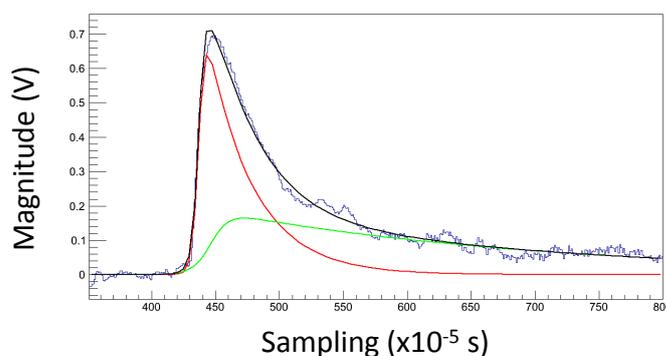
Fig. 16 - Typical pulse shape of the anticoincidence prototype 1 cm² area and 380 um thick. Risetime, fast and slow decay times are 24 us, 340 us, 12 ms respectively.

The photo-absorption efficiency for a nominal silicon anticoincidence 500 um thick decreases exponentially in the energy band 10-20 KeV as it can be seen in Fig. 17. On the other hand, the thermalization efficiency in silicon, i.e. the effective thermal energy η revealed in the pulse, is about 70% of the primary energy of radiation, because it is partially stored in the electron-hole long live metastable state at these temperatures. This is calculated as $\eta = 1 - (\delta/w)$, where δ=1.1 eV is the energy gap in silicon and w=3.4 eV is the average energy spent for creation of one electron-hole pair laying at the minimum energy state in the solid. Those electron-hole pairs diffuse in the crystal and recombine producing heat in a time scale much longer than the pulse length.
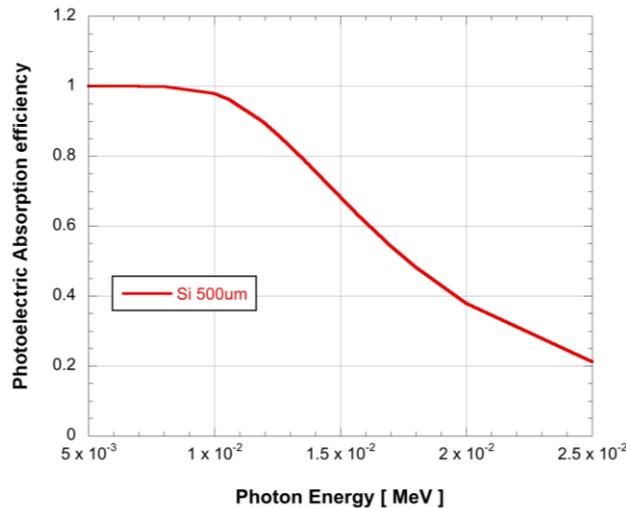
Fig. 17 - Photoelectron absorption efficiency in the 5-25 KeV band for the anticoincidence.

The physics of the electron-hole pair creation in silicon gives also an additional component to the intrinsic limit to energy resolution. Indeed this is given by the combination of two components: the electro-hole number fluctuation that goes as $(N_{e-h})^{1/2}=(EF\mathbf{w})^{1/2}$ (**F**, Fano factor = 0.1 in silicon) and the phonon number fluctuation that goes as $(kT^2C)^{1/2}$. In the Table 5, the expected intrinsic energy resolution for the anticoincidence prototype (made with electronic grade silicon) and the future spectroscopic prototype scaled at a reference area of 1 cm^2 (made with high purity silicon) at center of the band, i.e., 15 KeV are reported for comparison purpose.

Component	*Present Prototype*	*Future Prototype*
Absorber Volume	0.038 cm^3	0.050 cm^3
Silicon Type	electronic grade	intrinsic
Heat Capacity @ 0.1K	3.8 x10^{-10} J/K	2.5 x10^{-11} J/K
Pulse Amplitude @1uA TES bias, 15 KeV, 0.1K	1.5 x10^{-6} A	2.3 x10^{-5} A
Thermal time constant C/G (*measured*)	20 ms (*12 ms*)	1.3 ms
Johnson noise equivalent (1mΩ), BW=1MHz, FWHM, 0.1K	0.17 x10^{-6} A	0.17 x10^{-6} A
SQUID noise equivalent (VTT J3), BW=1MHz, FWHM,	0.085 x10^{-6} A	0.085 x10^{-6} A
Thermal Fluctuation Noise equivalent, BW=1MHz, FWHM, 0.1K	0.26 x10^{-6} A	0.42 x10^{-6} A
Total Noise equivalent FWHM, 0.1K	0.33 x10^{-6} A	0.45 x10^{-6} A
Energy resolution from e-h fluctuation noise FWHM	0.17 KeV	0.17 KeV
Total thermal energy resolution expected FWHM	3.3 KeV	0.30 keV
Combined e-h and Ther. En. resolution (*measured*) FWHM	3.3KeV (*7.9 KeV*)	0.35 KeV

Table 5 - Intrinsic energy resolution for the two study cases.

These values meet the requirements on the energy band and resolution. The efficiency is larger than 0.5 below 14 keV. Between 14 and 20 KeV it falls down from 0.8 to 0.4. This is acceptable in a complete trade-off process including the science cases. However, here we have also investigated two possible solutions that can increase the photoelectron absorption efficiency:

- increase the Silicon Thickness,
- grow metal film on to active area.

The first option allows to increase the efficiency to value greater than 0.4 at the highest energy of the 10-20 KeV band (Fig. 18). The saturation energy increases linearly, being heat capacity and deposited energy proportional to the absorber thickness t: $E_{sat} = \Delta T_{sat} C \propto \Delta_{sat} t$, where ΔT_{sat} is the maximum temperature swing to put the TES in normal state, i.e., in the saturation and **t** is the thickness. Then the anticoincidence performance remains unchanged, while the Hard-Xray sensitivity and resolution will be slightly worse (see Table 6).
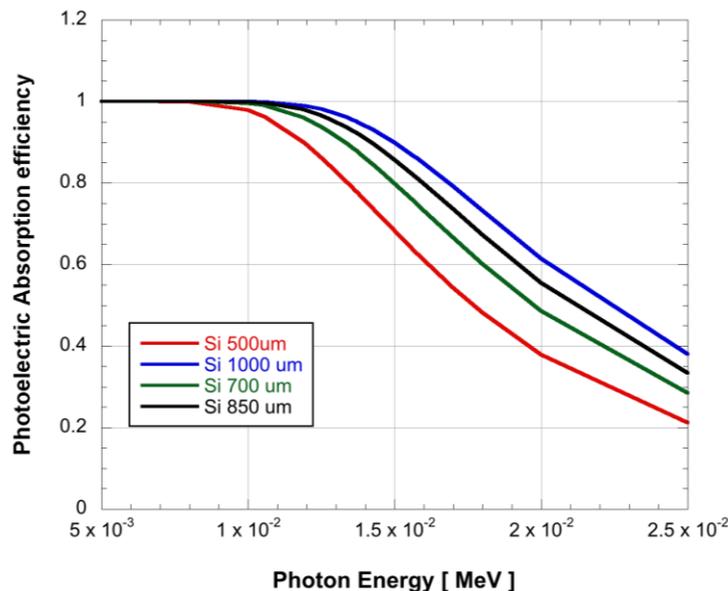
Fig. 18 - Photoelectron Absorption efficiency vs energy at several detector's thicknesses.

Component	*1 mm thick Option Prototype*
Absorber Volume	0.10 cm^2
Silicon Type	intrinsic
Heat Capacity @100mK	5.0 x10^{-11} J/K
Pulse Amplitude @1uA bias, 15 KeV	1.6 x10^{-5} A
Thermal time constant C/G (*measured*)	2.6 ms
Johnson noise equivalent (1mΩ), BW=1MHz, FWHM	0.17 x10^{-6} A
SQUID noise equivalent (VTT J3), BW=1MHz, FWHM	0.085 x10^{-6} A
Thermal Fluctuation Noise equivalent, BW=1MHz, FWHM	0.29 x10^{-6} A
Total Noise equivalent FWHM	0.33 x10^{-6} A
Energy resolution from e-h fluctuation noise FWHM	0.17 KeV
Total thermal energy resolution expected FWHM	0.32 keV
Combined e-h and Ther. En. resolution FWHM	0.36 KeV

Table 6 - Expected performance for 1 mm thick Silicon.

The second option has its main feature in creating a composite structure made by metal and silicon. The metal is grown directly on silicon onto the back side of the detector, i.e., the side opposite to the anticoincidence TESs.

The metal is primarily chosen to be normal conducting at the operating temperature. Actually a so large superconducting film can undertake mixed state and trap magnetic field with consequent negative effects on the TES sensitivity. The normal conducting film add a larger heat capacity but it is much easier to be simulated from the thermal and electromagnectic point of view, while the superconducting film needs a more complex study and experimental investigations. We have chosen as reference metals two high-z and high-ρ materials: Bi and W. Possible other metals can be taken under consideration in the study.

In the following Fig. 19 and Fig. 20 are shown the calculations for the photoelectron absorption efficiency for several thicknesses of Bi and W films grown onto silicon.
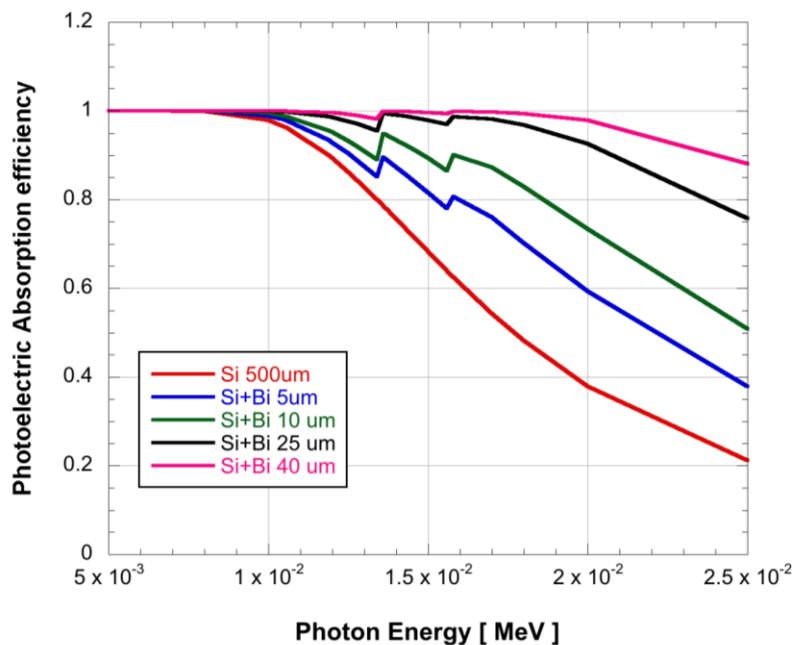
Fig. 19 - Photoelectron Absorption efficiency of a 500 um thick anticoincidence with Bi film of several thicknesses.

The photo-absorption efficiency is easily increased to value larger than 0.7 at 20 KeV with about 10 um of Bi or 6 um of W. Value larger than 0.9 require more than 15 and 25 um thickness of W and Bi, respectively. Special care must be addressed to the W film growth. Tungsten on the other hand remains normal conducting if it is grown in alpha phase. In Fig. 21 it is shown that alpha phase has been obtained at Genova onto Si-110 surface. The R vs T plot shows the absence of the other beta phase whose transition temperature is 3.2 K, while the alpha phase Tc=0.01K.

		WP6 CryoAC trade-off	**Doc. no.** : AHEAD-WP6-REP-004-2016
			Issue : 1
			Date : 03/10/2016
			Cat :
			Page : 28 of 38
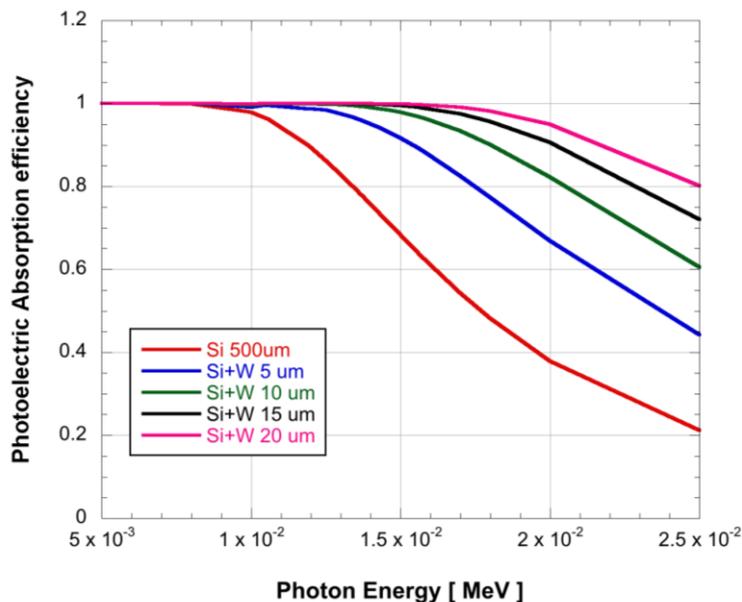
Fig. 20 - Photoelectron Absorption efficiency of a 500 um thick anticoincidence with W film of several thicknesses.
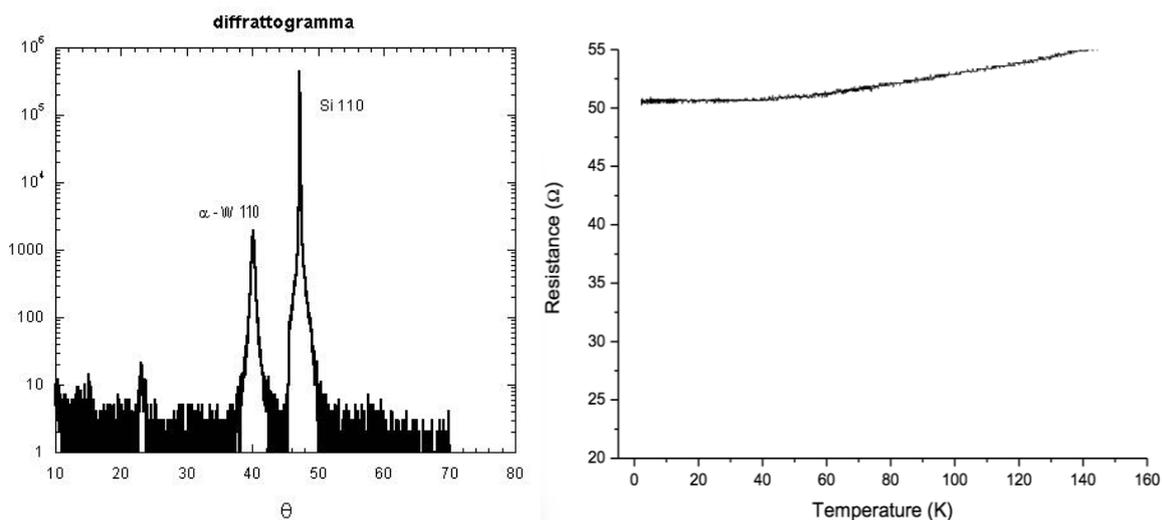
Fig. 21 - Xray diffraction pattern of thin W film grown onto Si 110 with pulsed laser deposition at Genova (left) where the alpha phase is very well recognized and the resistance measurement down to 1.3 K (right).

There are two main drawbacks of this last option: (a) the prevailing contribution to the heat capacity of the metal film, (b) the possible presence of replica of the X-ray lines due to different thermalization efficiency in metal and silicon.

Metal film	Thickness & Heat Capacity 60% eff. At 20 KeV	Thickness & Heat Capacity 80% eff. At 20 KeV	Thickness & Heat Capacity 90% eff. At 20 KeV
Bi	5 um - 5 x10^{-10} J/K	15 um – 1.5 x10^{-9} J/K	25 um - 2.5 x10^{-9} J/K
W	3 um - 6 x10^{-9} J/K	10 um - 1.4 x10^{-8} J/K	20 um – 1.9 x10^{-8} J/K

Table 7 - Thickness and Heat Capacity for different absorption efficiency evaluated for Bi and W.

The Table 7 shows that Bi is more convenient than W, having a heat capacity 10 times lower at the same absorption efficiency and slightly greater thicknesses. In addition, the Bi heat capacity for 40% efficiency is more than one order magnitude larger than the 1 mm silicon detector. An overall worsening of performance should be experienced.

The second drawback is the possible presence of ghost replica of the x-ray lines due to different thermalization efficiency in metal and in silicon. The X-ray energy absorbed in metal goes almost completely (about 100%) in heat to the electrons gas. The electron gas then releases heat in silicon generating the heat pulse. On the other hands, as seen before, in silicon the electron-hole pairs retain almost 30% of the X-ray energy for very long time. Only the 70% of the primary energy gives rise to the prompt heat pulse. For example, this means that in a detector Si-500um+Bi-7um an X-ray line at 20 KeV should give two "instrumental" lines: (a) a first line corresponding to the absorption in Bismuth and (b) a second line apparently at 14 keV due to the absorption in silicon (Fig. 22). The presence of this replica can be easily predicted with simple models but must be experimentally verified. If confirmed, this is the major disadvantage of using a composite structure metal-silicon. Indeed, this will generate instrumental spectral artefacts over the genuine astrophysical spectra.
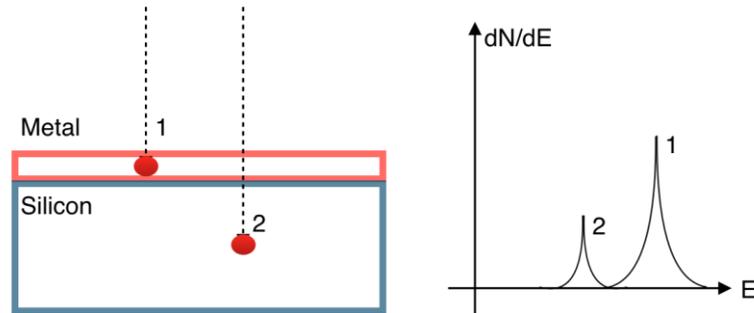
Fig. 22 - In a detector with Metal-Silicon structure an x-ray at energy E$_1$ should give two lines: (1) one line corresponding to the absorption in metal and (2) a second line apparently at E$_2$= 0.7E$_1$, due to the absorption in silicon, where the thermalization efficiency is about 0.7.

4.2   Concept design #2

This is based on the expertise in using High-Z, High- ρ superconducting absorbers like Iridium, Rhenium, Tungsten. In these cases Z are 74, 75 and 77 and ρ from 22.5, 22.1,19.3 g/cm³, respectively. In the early investigations about the capability of superconductors to efficiently absorb the primary energy of the radiation and down-convert promptly to heat, i.e. thermalization process, those materials were very attractive because of the very low heat capacity at T<<Tc. This is due to the almost full condensation of almost all the quasi-particles at so low temperatures so that the Debye term of specific heat becomes dominant. The results of many experiments by several groups have shown that the phenomenology of the thermalization process of the radiation energy in the superconductors is complex and quite diversified among various superconductors. Here we do not enter in the physical details that perhaps are not fully explained despite many experimental and theoretical efforts. However, at very first approximation, we can share the most common superconductors in two classes: "soft" or low Debye temperature ones (Sn, Pb, In,…) that show a quasi-complete thermalization in short time scale, "hard" or high Debye temperature ones (Re, W, Nb…) that have larger time scale thermalization. This means that the latter class of superconductors show typical response pulses to single X-ray absorptions with two main decay components. The first quite fast and the second one very long, i.e. tens of milliseconds typically at 0.1 K. However, this problem does not prevent the use of these superconductors because many good results have been obtained in the past in X-ray spectroscopy. As an example in the following figure (Fig. 23) it is shown the spectrum in the hard X-ray bad obtained with Re crystal of 0.5 x 0.5 x 0.5 mm³ volume [RD9] while Fig. 24 shows the Rhenium photo-absorption efficiency as function of energies at several thicknesses. At a reference thickness of 30 um the detection efficiency is greater than 98% over the 10-20 keV band.
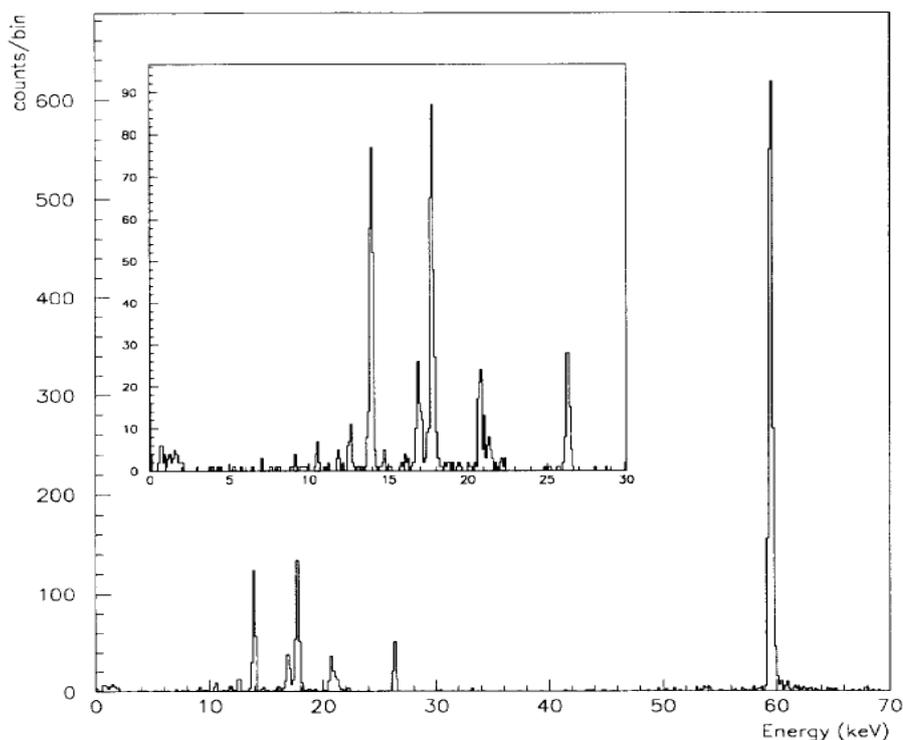
Fig. 23 - The spectrum in the hard X-ray bad obtained with Re crystal of 0.5 x 0.5 x 0.5 mm³ volume.

The energy resolution in the 10-30 KeV range was better than 0.3 KeV FWHM at a temperature of 150 mK. Rhenium in particular, or some superconductor with similar properties, i.e. Os, looks very appealing for many reasons, even if it exhibits a long tail in the pulse recovery time:

1) Very short photo-absorption depth: 10-20 um
2) L3, L2, L1 line at 10.5, 12.0, 12.5 KeV respectively, M lines below 2.9 KeV
3) Linear response over 60 keV (non linearity at level of $<10^{-3}$)
4) Reasonable good energy resolution in the hard X-ray (about 0.3 keV FWHM))
5) Physically and chemically very stable material over long time
6) A small excess of effective specific heat found T<<Tc when measured with radiation: the measured value with 60 keV X-ray is about 30 pJ/Kmm^3
7) Re contains Re-187 isotope that decay with beta (electron) transition to ground state of Os-187 (no gamma emission) and a maximum energy of 2.45 KeV. The half-life is about 45 Gy therefore there will be few tens of beta (electron) decay per mm^3 and per second of average energy of 0.8 KeV.
8) Very well studied, easy to be machined (cut with wire of circular saw) and lapped.
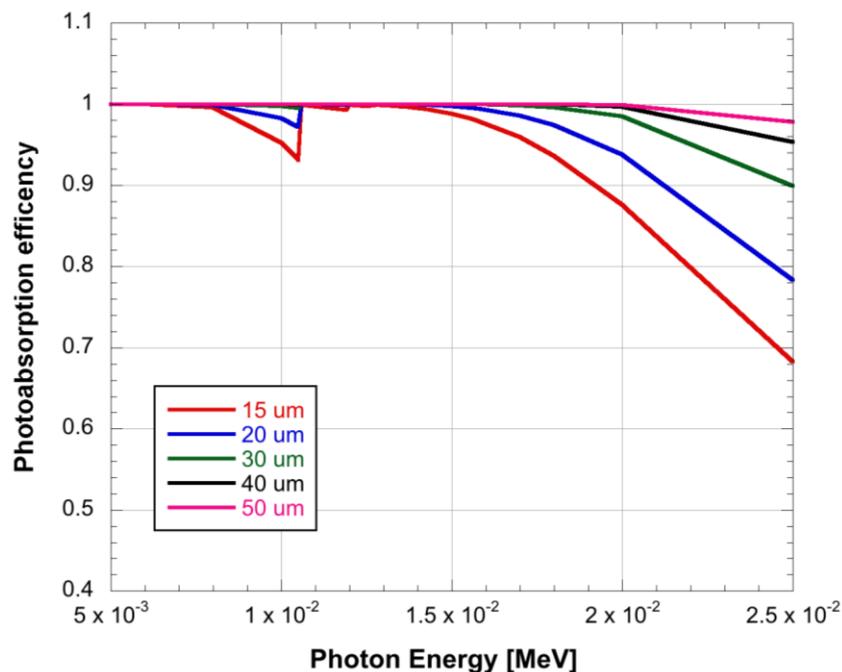
Fig. 24 - The photo-absorption efficiency as function of energies at several Re sheet thicknesses ranging from 15 to 50 um. With a thickness of 30 um it is possible to have more than 98% from 10 to 20 keV.

These properties can meet very well the following conceptual design (Fig. 25) of the anticoincidence with hard-X-ray sensing capability.
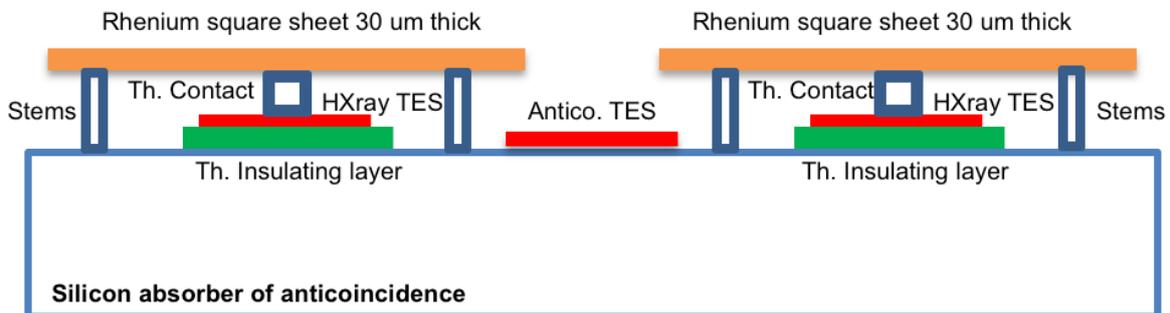
Fig. 25 - Scheme of the Hard-Xray upgraded of anticoincidence in conceptual design 3. This will require a second multi-TES readout channel. The first channel is dedicated to the anticoincidence primary signal. Square sheets of Re 30 um thick (orange) should detect the 5 to 20 keV x-ray with efficiency higher than 90%. The thermal signal from Re is readout by the second TES(red) channel. Being the signal from rhenium longer than the one of anticoincidence, for the best matching, this is grown on top of slightly insulating layer (green).

The anticoincidence detector is extended with a new layer made be contiguous square sheets of Rhenium, or similar superconductor, at few tens of micrometres from the original TES. The Rhenium sheets are strongly connected to a second array of TESs, parallel connected, for their temperature reading. Because the Rhenium dynamical response to an excitation is quite different from the anticoincidence, due to its typical internal longer thermalization times, the thermal contacts Rhenium-TES and TES-Silicon must be chosen in careful way to reach the best signal amplitude. Further pillars (or stem) are necessary to have a stable structure. Indeed, with a volume of 0.12 mm^3 of Rhenium and a thickness of 30 um the square pixel size is about 2 mm, i.e. 4 mm^2 area. In principle pixel sizes of 3-4 mm, i.e. 9-16 mm^2 area, appear feasible. Then, with the optimal pixel size of 2 mm, each anticoincidence pixel of 1 cm^2 area will need about 25 hard X-ray pixels arranged in one single electronic channel by reading the corresponding 25 TES in parallel. A smaller number of TES could be designed if detailed study will permit to move toward the 3-4 mm pixel size without unacceptable performance loss. In this case the number of hard X-ray pixels could be about 10 or less, leading to great design simplification (Fig. 26, Fig. 27).
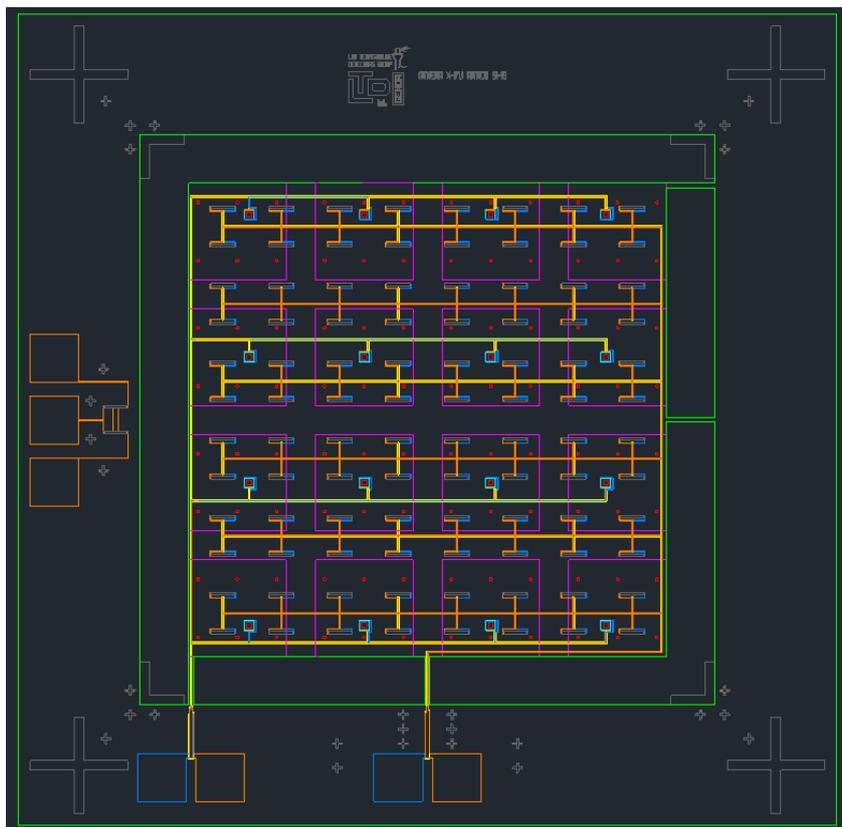
Fig. 26 - CAD drawing of the full set of the micro-lithography masks for the concept design #2.
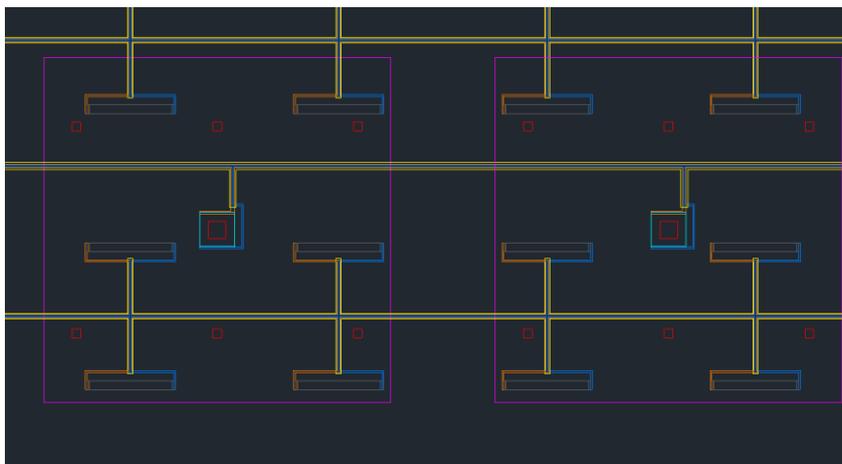
Fig. 27 - Particular of the CAD drawing of the full set of the micro-lithography masks for the concept design #2. Squares of cyan colour: superconducting absorber sheets; small red squares: supporting pillars; centred blue/red squares: Hard X-ray TES and stem, wiring for parallel connection of all TESs. The 2nd layer structure of the Hard X-ray component fit well in the anticoincidence TES configuration.

The thermal model and the parameter evaluation table based on current available date are drawn below (Table 8 and Fig. 28).

Parameter	Evaluated value	Parameter	Evaluated value
C(S/c.Abs.) (Re)	4 pJ/K @ 100 mK	G(TES-Si)(elec.-Phon.)	2×10^{-10} W/K @ 100 mK
G(Stem S/c Abs – TES))	TBD in this project	C(Antico TES)	3×10^{-14} J/K @100 mK
C(Hxray TES)	5×10^{-2} pJ/K @ 100 mK	C(Silicon Absorber)	2×10^{-10} J/K @100 mK
G(S/c.Abs-Ins-Si)	TBD in this project	G(Antico Si – Legs)	4×10^{-8} W/K @100 mK

Table 8 - Parameter evaluation of the Concept Design #2.
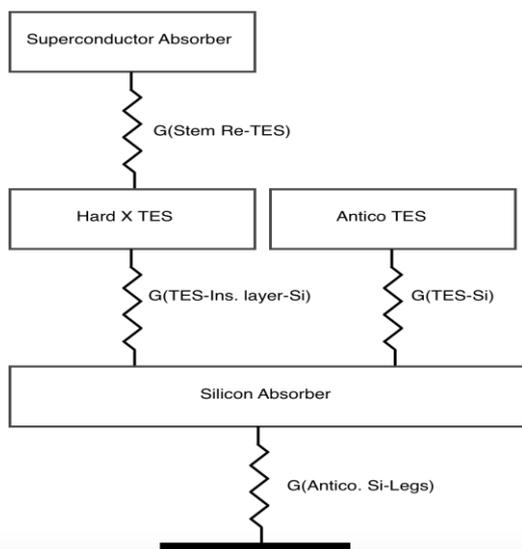
Fig. 28 - Thermal model of the concept design CD#2.

4.3 Conclusion of the technological study

We have investigated 2 main conceptual designs CD#1 and CD#2 for the upgrade of the anticoincidence silicon detector as it is now conceived for the XIFU instrument of the ATHENA mission.

The CD#1 has 2 possible configurations: all silicon and metal-silicon composite structure.
The CD#2 is made of an array of dedicated detector based on superconducting high-Z & high-ρ large crystal sheets readout by a dedicate new electronic channel. For a simple comparison we have used a reference area of 1cm^2. In the Table 9 below are listed le main parameters for a comparison.

Parameter	CD#1 all silicon	CD#1 metal-silicon	CD#2
Detection efficiency 500 um Si	0.95@10KeV 0.38@20KeV	1.0@10KeV 0.6@20KeV Bi- 5 um	1@10KeV 0.98@20KeV Re 30 um x (2 x 2) mm^2
Detection efficiency 1000 um Si	1.0@10KeV 0.6@20KeV		
Intrinsic Energy Resolution 500 um Si	0.35 keV FWHM	10KeV FWHM	< 0.3 keV
Intrinsic Energy Resolution 1000 um Si	0.36 KeV FWHM		
Technical readiness	Very good (limited further studies, silicon quality selection)	Good (film Bi and W growth test and characterization done)	Poor (only one single pixel test available)
Possible difficult issue	Very Deep Etching of 1 mm silicon need special attention: process to be fixed.	Xray line duplication problem.	Tailoring heat capacities and thermal conductance. All fab processes to be fixed.
Detector Parameter Knowledge	Almost done for all. Conductance and Heat capacity of silicon to be fine tuned.	Almost done for all. Conductance and Heat Capacity of silicon to be fine tuned. Effective heat capacity of metal film to be verified.	Not yet done for the suspended Re crystal structure and thermal connection Re-TES and TE-Silicon.

Table 9 – Comparison among the main parameters of Concept Design #1 and #2.

The conclusion of this investigation is summarized as follow.

The CD#1 in all silicon configuration meets the requirement for covering the 10-20 keV band with energy resolution largely better than 2keV and the detection efficiency exactly to the requirement of $\geq$ 40% at the high edge of the energy band. This can be increased to about 60% with doubling the thickness to about 1mm or tuned to intermediate values adjusting the thickness. The consequent energy resolution worsening is acceptable and however within the requirement. The configuration Metal-Silicon can reach very high efficiency at expenses of additional huge heat capacity. In the minimal configuration for 60% detection efficiency at 20 keV a thin layer of 5 um of Bi is necessary with a corresponding increase of more than 1 order of magnitude of heat

capacity. In case of W the additional heat capacity is 2 orders of magnitude larger. So that, we can conclude that the metal-silicon configuration has poor performance and produce spectral artefacts. This effect is quite pernicious for a correct spectral analysis.

The CD#2 meets all the requirement and can reach good energy resolution better than 0.3 keV and very high detection efficiency. Further, the dedicated electronic chain allows to disentangle among different origin of the events and a very good discrimination by using the differences in pulse shapes of X-ray from GeV proton event. Coincidence with the silicon sub detectors and an easier analysis can be done. This solution, on the other hand, for its low technical readiness needs detailed study to define fabrication processes and special technical solutions for the thermal insulation of the related TES from the silicon absorber (Fig. 25). Further, a fine tuning of all heat capacities and thermal conductances (see model of Fig. 28) is necessary for a proper operation.

5 Impact at the ATHENA X-IFU system level by adopting a "spectroscopic" CryoAC

In this section we will report what could be the impact at the X-IFU system level if a spectroscopic CryoAC would be adopted.

The main parameter to be probed are:

- Expected increase of the bit rate
- CD#1 vs CD#2

Other items such as thermal control, magnetic shieldings, etc. probed by the instrument team to optimize the TES-array operation are considered adequate for the CryoAC being the last less demanding in terms of energy resolution.

5.1 Expected increase of the bit rate

Usually for a HMXB we expect for the CryoAC a count rate of ~ 10 cts/s (see Fig. 12), this means ~ 3 cts/s/pixel (10-20 keV bandwidth) being the CryoAC divided in 4 pixels. This increases of about 30% the bit rate of the CryoAC from ~ 4 kbit/s to ~ 5 kbit/s (in case of only GCR we expect among primaries and secondaries ~ 10 cts/s/pixel). In case this increase should be considered high, we could envisage a sort of "CryoAC Scientific mode" of operation in order to allocate from the system adequate bandwidth only when necessary.

On the other hand, given the expected CryoAC maximum energy (< 1 MeV), the 16 allocated bit related to the "Amplitude" in the CryoAC event size for Science telemetry provide a resolution ~ 15 eV/bit which is adequate for sampling the pulse amplitude in order to perform spectroscopy (expected 1-sigma noise ~ 150 eV).

5.2 CD#1 vs CD#2

The main difference between the two designs is that the CD#2 requires an addictive readout chain, being the CD#1 just an improvement of the CryoAC baseline detector in term of the absorber.

6   Conclusions

In this trade-off report we have probed if the CryoAC is able to perform "science", and the possible technological solution to be implemented, as well as possible impact at system level, to improve its scientific performances.

Due to the ATHENA optics effective area limited to around 20 keV (< 1 cm^2), in order to increase the CryoAC sensitivity the main focus of the improvement is the energy resolution rather than the quantum efficiency that is good at this energy range being the baseline CryoAC absorber made of 500 µm silicon thick. For completeness, we have however provided also a study on how to improve the energy bandwidth, interesting for development beyond ATHENA.

By taking into account the Aeff, the X-ray thermal filters and TES-array absorption, we have estimated both the CryoAC minimum detectable flux and the continuum sensitivity. The particle background has been evaluated by means of the TES-array "reversing" the usual operation performed by definition through the CryoAC (it will be an on-ground operation). Then, by XSPEC, we have simulated a class of object for which we could expect a scientific contribution by the CryoAC (HMXB as study case), so arriving at the **requirement of 2 keV (FWHM) in 10 - ~20 keV energy bandwidth**. Quite important, we have seen in the ATHENA Mock Observing Plan that there are about 35 sources with characteristics similar to the ones we have simulated, so enforcing the CryoAC as possible scientific instrument.

Hence, it has been studied how it is possible to face this requirement from the technological point of view by proposing two designs: CD#1 and CD#2.
From CD#1, roughly, by a proper selection of the Silicon absorbers, it is possible to improve the energy resolution to 0.35 keV (FWHM@15keV) without modifying the CryoAC baseline detector design.
Further, in case of absorption efficiency improvement at fixed geometry, with an a) increase of the Si thickness to 1000 um or, b) grow metal film on to active area, it is possible to reach an efficiency of ~ 0.6 (20 keV) but with the drawback of problematic energy spectrum identification for case b) due to X-ray line duplication issue caused by different thermalization efficiency in Silicon(70%) and in metal(100%).
The CD#2 solution merges the good energy resolution (better than 0.3 keV FWHM) with a high quantum efficiency of 0.98 (20 keV). It foresees the fabrication of a few ten's TES detector matrix coupled with "Superconducting-Rhenium" absorbers (30 um thick 2x2 mm^2) using the present CryoAC as supporting frame and thermal link to the sink. The technical readiness of this solution is at present poor, and further detailed studies and experimental measurement are needed to verify the concept feasibility.

Being possible to reach the requirement from the technological point of view we have, at last, studied what could be the impact at the X-IFU system level having a "spectroscopic" CryoAC.
Two main parameters have been analyzed: Expected increase of the bit rate; CD#1 vs CD#2.
About the bit-rate we expect a slight increase of the amount, from ~ 4 kbit/s to ~ 5 kbit/s, for which we could however envisage a sort of "Scientific mode" of operation in order to allocate from the system adequate bandwidth.
About the CD#1 vs CD#2, the main difference between the impact is that the CD#2 requires an addictive readout chain, being the CD#1 just an improvement of the CryoAC baseline detector in term of the absorber.

The main conclusion of this trade-off study is that with a moderate technological development, we could provide a "spectroscopic" CryoAC detector providing scientific results for tens of sources already present in the ATHENA Mock Observing Plan. Hence, this solution could be recommended to the X-IFU science team to start a discussion on this item.